DOI: 10.13009/EUCASS2023-712
Aerospace Europe Conference 2023 – 10TH EUCASS – 9TH CEAS

Estimation of Hard Start Mechanism by Visualization Test of Hypergolic Bipropellant Thruster

Kohji Tominaga †, Yu Daimon *, Go Fujii *, Taiichi Nagata *, Yoshiki Matsuura **, Yasuhito Kano **, and Erika Uchiyama ***

** Japan Aerospace Exploration Agency (JAXA)*

2-1-1 Sengen, Tsukuba City, Ibaraki, Japan

† Corresponding Author

tominaga.kohji@jaxa.jp – daimon.yu@jaxa.jp – fujii.go@jaxa.jp – nagata.taiichi@jaxa.jp

*** IHI AEROSPACE Co., Ltd.,*

900 Fujiki, Tomioka, Japan,

yoshiki-matuura@iac.ihi.co.jp – yasuhito-kano@iac.ihi.co.jp – erika-uchiyama@iac.ihi.co.jp

Abstract

The process of hard-start generation, an unstable starting mode for bipropellant thrusters, was estimated through a visualized firing test using a thruster with a visualized combustion chamber. It was clarified that combustion chamber pressure and hard start are strongly linked. Flash boiling of the oxidizer in a vacuum environment causes a prolonged ignition delay. Ignition occurs when the combustion chamber pressure rises above the oxidizer vapor pressure due to the reaction gas. At that time, unburned fuel accumulates in the combustion chamber, causing detonation with high intensity and high propagation velocity immediately after ignition.

1. Introduction

Bipropellant thrusters for spacecraft have higher specific impulse than monopropellant thrusters and can generate larger thrust. The most common propellant combination is dinitrogen tetroxide containing 3 wt% NO (MON-3) as the oxidizer and either hydrazine (N2H4) or monomethyl hydrazine (MMH) as the fuel [1,2]. This combination of propellants is classified as a hypergolic propellant, which means it spontaneously ignites a combustion reaction when brought into contact with the propellants. However, the ignition process in a bipropellant thruster is a very complicated phenomenon because of the multiphase flow of the multi-component system including condensed phase reactions [3,4]. During start up of bipropellant thrusters in a high vacuum environment, unstable ignition events such as hard start may occur [5,6]. Hard start is an ignition caused by a sudden increase in combustion chamber pressure, which can cause catastrophic damage to the thruster and combustion instability [7-9]. The occurrence of hard start has been reported in previous engine development tests, and its excessive pressure intensity has become a major problem [10]. Recently, hard start has been successfully observed in test thrusters using high-speed visualization techniques, but the detailed mechanism of hard start remains unknown [11,12]. Therefore, understanding the transient phenomena up to the hard start is extremely important to improve the performance and reliability of spacecraft propulsion systems.

Hard start is empirically considered to be caused by the accumulation of unburned fuel in the combustion chamber during start up [13,14]. Unburned fuel accumulation is caused by environmental factors in the combustion chamber that increase the length of the ignition time delay. In previous studies, heat absorption effects in the injector have been reported to cause gas-liquid two-phase flow in the MON-3, which can destabilize the ignition and combustion conditions [15]. It has also been suggested that when the combustion chamber pressure, which is equivalent to the injector back pressure, is low, MON-3 with high saturated vapor pressure may also induce ignition instability due to flash boiling injection [16]. Therefore, the parameters governing the mixing and atomization of heterogeneous impacts, such as liquid phase fraction and momentum ratio [17-19], may change, and the mixing and atomization conditions may not be suitable for ignition. Therefore, detailed understanding of the propellant flow and ignition conditions inside the combustion chamber during the transient process of hard start is important to clarify the mechanism of the hard start.

The objective of this study is to clarify the scenario of hard start by observing the physical phenomena during the start transient in bipropellant thrusters. High-speed observations of the ignition process and combustion chamber pressure measurements using a visualized combustion chamber are performed to observe the propellant flow state and flame development. In addition, the combustion conditions in the combustion chamber and in the pressure conduit during the hard start of the ignition process are evaluated by numerical simulation and compared with the combustion chamber

DOI: 10.13009/EUCASS2023-712

pressure to clarify the combustion pattern of the ignition impact. Based on these results, a scenario from the start of propellant supply to the hard start was estimated. By clarifying the transient physical phenomena during the hard start of a bipropellant thruster, it is possible to design a thruster with a reduced probability of hard start.

2. Experimental and Analysis procedure

2.1 Firing test using visualized combustion chamber

To observe the propellant flow state and the occurrence of hard start, a firing test was conducted using a bipropellant thruster with a visualized combustion chamber. **Figure 1** shows a schematic diagram of the visualization test apparatus and the setup for high-speed visualization measurements. The visualized firing test apparatus shown in **Figures 1(a) and (b)** consists of a propellant valve, injector, visualized combustion chamber, nozzle and throat sections, and pressure ports. N2H4/ MON-3 was used as fuel and oxidizer. Typical properties are shown in **Table 1**. Firing tests were conducted by injecting MON-3(O) and N2H4(F) into the combustion chamber through the injector by controlling the propellant valve ON/OFF. Two visualized combustion chambers were fabricated: a rectangular combustion chamber with quartz glass front and rear surfaces for easy optical observation of the internal conditions, and a cylindrical combustion chamber for detailed confirmation of the combustion chamber pressure conditions. The longitudinal lengths of the visualized combustion chambers were 48 mm and 30 mm, respectively. A vacuum pump was connected downstream of the nozzle to control the combustion chamber pressure Pc_{ini} before the propellant valve ON.

Figure 1(c) shows the optical setup image. Two high-speed cameras were installed to observe the propellant flow and combustion conditions in the combustion chamber. CAM1 (Photron FASTCAM NOVA S16) captured images of the wall propellant conditions and self-luminous by burning in the entire combustion chamber, while CAM2 (Photron FASTCAM SA-Z) captured images of the propellant jet and spray near the injector using a high-intensity light source on the opposite side of the combustion chamber as backlight. The frame rates were set to 25,000 fps and 40,000 fps, respectively. The combustion chamber pressure Pc was measured at 2000 Hz by a pressure sensor (KYOWA PHL-B-3MP) through a pressure port 50 mm from the combustion chamber. Fuel inlet pressure (PIF) and oxidizer inlet pressure (PIO) were measured with a pressure sensor (KYOWA PHL-B-3MP) 500 mm upstream of each propellant valve.

The configuration of the injector is shown in **Figure 1(d)** and the design parameters are listed in **Table 2**. The injector used in this test is a unlike impinging type injector with two OF elements and two F-film cooling orifices. The design parameters of the injector were selected to have an orifice diameter capable of producing a thrust of 20 N class. A film-cooling orifice is provided for the main combustion flame, considering the influence of the film cooling on the flame. In addition, the number of orifices was set to easily visualize the inner condition. High-speed cameras CAM1 and CAM2 were used to capture images of the fuel jet F and oxidizer jet O from the front of the plane and from the front-back direction parallel to the fan plane. The film-cooled FC was placed perpendicular to the plane of the fuel and oxidizer jets with a phase difference of 90°.

Typical CAM1 and CAM2 visualization images are shown in **Figure 2**. **Figure 2(a)** shows a representative CAM2 visualization image at the start of O injection, where only the oxidizer is injected for a certain period because the manifold volume of O is smaller than that of F and the injection timing is earlier from the propellant valve opening. **Figure 2(b)** is a representative example of a CAM2 visualization image of F and FC following O at the start of injection. The FC is visible on the front side toward the downstream center, and it can be confirmed that many droplets are formed by the impingement of O and F. Figure 2(c) is a typical CAM1 visualization image. The state of the propellant flowing on the wall and the flame condition can be confirmed.

The conditions of the firing test are shown in **Table 3**. The parameters were mass flow rates Q_O and Q_F, and the combustion chamber pressure before injection start Pc_{ini}. They were adjusted by adjusting the propellant tank pressure and the vacuum level using a vacuum pump. The mass flow rate Q_O and Q_F were adjusted about 12N (low flow rate) to 22 N (high flow rate), and the combustion chamber pressure Pc_{ini}, was adjusted between 0.001 MPaA and 0.12 MPaA to achieve the desired values. The mixing ratio ($MR = Q_O / Q_F$) was set to $MR = 0.8$. To reduce the heat load on the combustion chamber, the injection time was set to 50 ms and 100 ms for the rectangular combustion chamber and 50 ms for the cylindrical combustion chamber.

Table 1 Physical properties of propellants

Propellant	Molecular weight M, g/mol	Density ρ, g/m^3	Vapor pressure P_v, MPaA
Dinitrogen tetroxide (N_2O_4)	92	1433	9.60×10^{-2}
Hydrazine (N_2H_4)	32	1003.6	1.92×10^{-3}

DOI: 10.13009/EUCASS2023-712

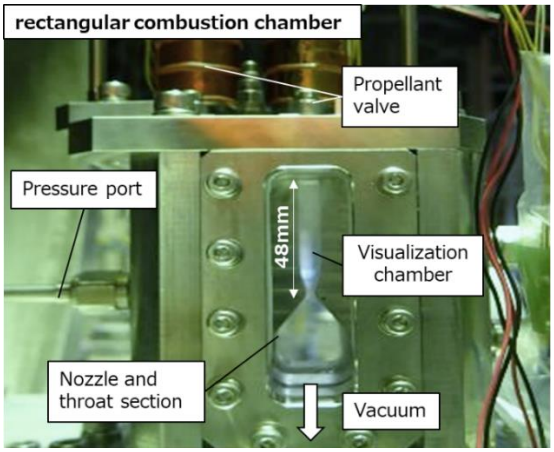

(a) rectangular visualized combustion chamber setup

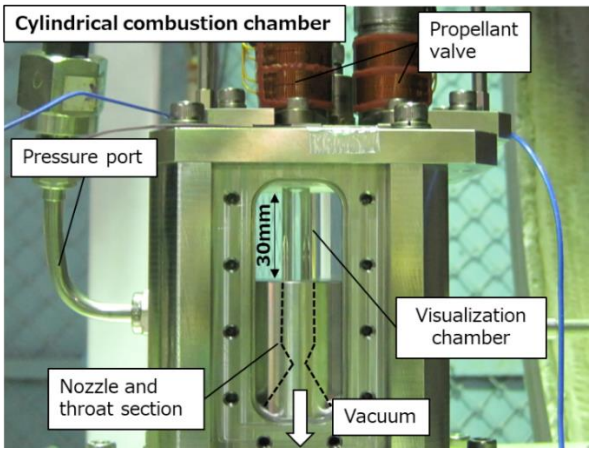

(b) Cylindrical visualized combustion chamber setup

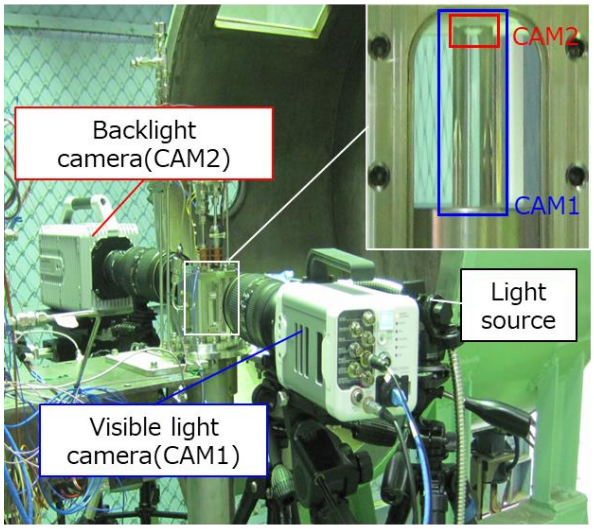

(c) Optical measurement device setup

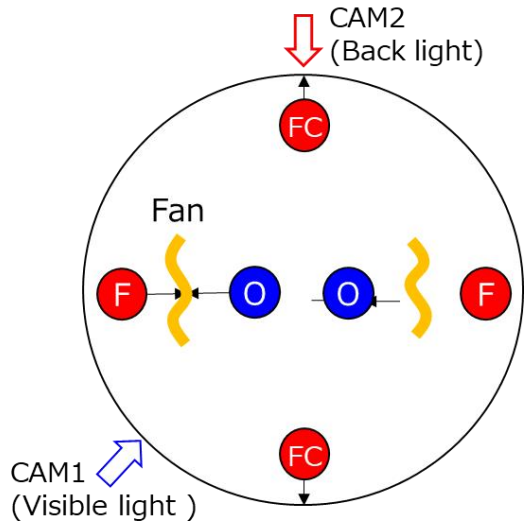

(d) Injector configuration

Figure.1 Combustion test setup with visualized firing chamber

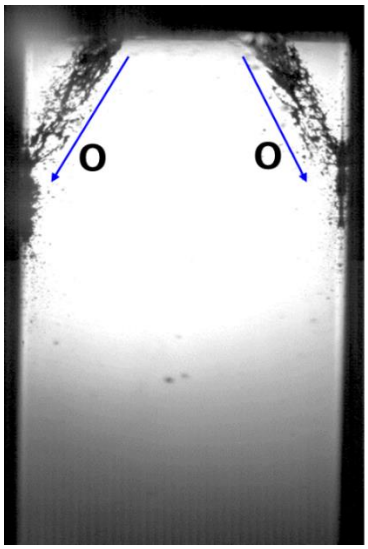

(a) O injection just after propellant valve opening (CAM2)

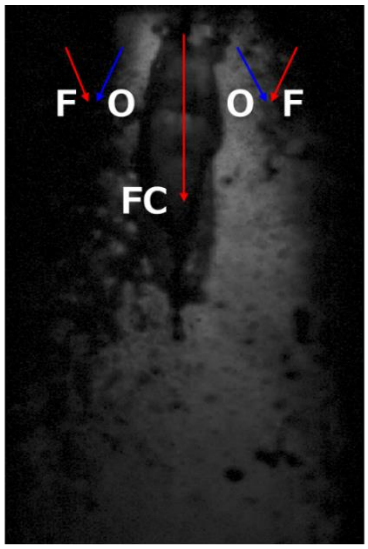

(b) F and FC injection with O (CAM2)

(c) Combustion conditions (CAM1)

Figure.2 Typical high speed visualization images with CAM1 and CAM2

DOI: 10.13009/EUCASS2023-712

Table 2 Injector design parameters

	Propellant -	Element -	Orifice diameter *d*, mm	Reynolds number *Re*, -	Weber number *We*, -	Orifice L/D L/D, -
F	Hydrazine	2	0.28	5.3×10^3	1.3×10^3	About 5
O	MON-3	2	0.29	1.7×10^4	5.0×10^3	About 5
FC	Hydrazine	2	0.25	-	-	-

Table 3 Test conditions

Test case	Flow rate *Q*, g/s	initial chamber pressure Pc_{ini}, MPaA	Mixing ratio *MR*, -	ON time t_{on}, ms	Chamber type -
Case 1	(F) 3.3, (O) 2.6 * Nominal	0.1	0.8	50	Rectangle
Case 2	(F) 3.8, (O) 3.0 * High	0.1	0.8	100	Rectangle
Case 3	(F) 2.4, (O) 1.9 * Low	0.12	0.8	50	Rectangle
Case 4	Nominal	0.12	0.8	50	Rectangle
Case 5	Nominal	0.08	0.8	100	Rectangle
Case 6	Low	0.08	0.8	50	Rectangle
Case 7	Low	0.11	0.8	50	Rectangle
Case 8	Low	0.08	0.8	50	Rectangle
Case 9	High	> 0.001	0.8	50	Cylindrical
Case 10	Low	> 0.001	0.8	50	Cylindrical
Case 11	High	> 0.001	0.8	50	Cylindrical
Case 12	High	> 0.001	0.8	50	Cylindrical

2.2 Numerical combustion analysis inside combustion chamber and pressure ports

Computational Fluid Dynamics (CFD) analysis was performed in the combustion chamber and pressure port to reproduce the combustion conditions during a hard start. Ansys Fluent®, a general-purpose fluid analysis software, was used for modelling and analysis. **Figure 3** shows the computational domain and boundary conditions. A part of the combustion chamber and the entire inside of the pressure port were used as the computational domain. The pressure port has a volume several times larger than the combustion chamber, and a pressure sensor is installed at its end. The lattice spacing was set to 0.001 mm at the first layer of the entire wall. The combustion chamber and joints were set at 0.1 mm with an aspect ratio of 1, and the pressure port was set at 0.1-1.9 mm with an aspect ratio of 1-20 in the direction of the pressure measurement area. The walls of the combustion chamber and pressure conduit were insulated and no-slip. The test conditions for comparison were the results of a combustion test using a cylindrical combustion chamber with a flow rate equivalent to 22 N and Pc_{ini} = 0.001 MPa. Since information on detonation in the combustion chamber was required for the initial conditions, the ZND detonation pressure, temperature, and composition calculated by NASA CEA [20] were specified based on the pre-ignition pressure and temperature data from the combustion test results. The combustion chamber outlet pressure was fixed at 10 Pa.

Two types of analysis were performed. Figure 4 shows the conditions inside the pressure port. In the first case, the analysis assumes that detonation occurs inside the combustion chamber and that the shock wave propagates into the pressure port with attenuation. To simplify the analysis, detonation was assumed to propagate instantaneously, and the state behind the detonation was assumed to be a high-pressure section attached to the combustion chamber to analyse the propagation of the generated shock wave. In the second case, a combustion analysis was conducted assuming that premixed gas existed up to the middle of the pressure port. This is referred to as the combustion analysis case. The premixed gas in the pressure conduit was set to 1/4 and 1/2 volume conditions, and the remaining area was filled with oxidizer gas. The governing equation is a two-dimensional axisymmetric compressible N-S equation. Second-order accurate central differencing was selected for the spatial differencing for the pressure equation, second-order accurate upwind differencing for the other equations, and second-order accurate implicit integration for the time integration. As a reaction model, a finite rate reaction analysis was performed for 268 elementary reactions of 39 chemical species [21], which were reduced to 181 elementary reactions of 27 chemical species.

DOI: 10.13009/EUCASS2023-712

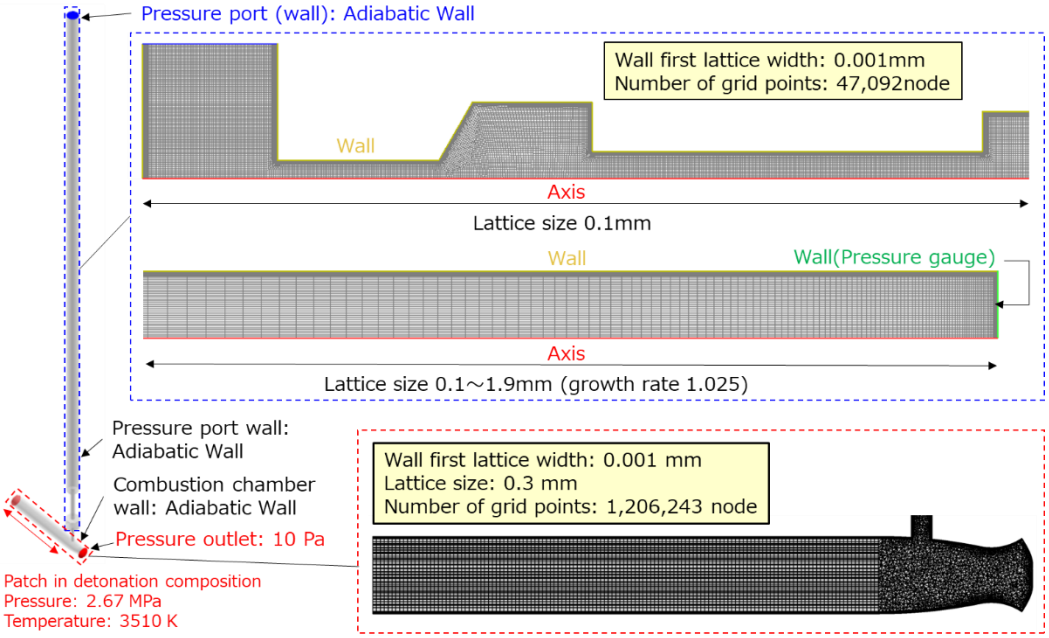

Figure.3 Modeling of combustion chamber and pressure port for CFD analysis

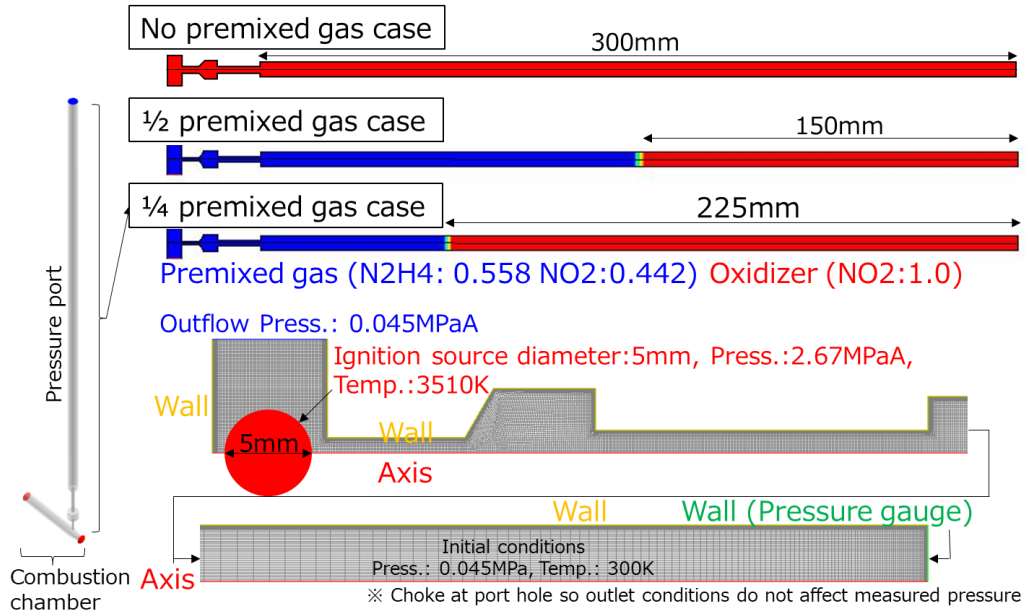

Figure. 4 Premixed gas introduction conditions and initial conditions in the analysis

3. Results and Discussion

3.1 Classification of hard start and normal ignition

First, the classification of normal ignition and hard start is shown. **Figure 5** shows a comparison of inlet pressure and combustion chamber pressure histories obtained from firing tests using a rectangular combustion chamber under two conditions: a high initial chamber pressure case with an initial pressure of Pc_{ini} = 0.1 MPaA (Case 2) and a low initial chamber pressure case with an initial pressure of Pc_{ini} = 0.08 MPaA (Case 5). The time of the propellant valve ON signal for O and F was set to 0 ms. For the high initial chamber pressure case in **Figure 5(a)**, a pressure increase was

DOI: 10.13009/EUCASS2023-712

observed around 17 ms after the propellant valve was opened, confirming that ignition had occurred. The pressure was roughly steady for about 50 ms after that, confirming that the flame was maintained. For the low initial chamber pressure case in **Figure 5(b)**, a rapid pressure increase was observed at 57.5 ms after the propellant valve was opened, confirming that ignition had occurred. Immediately after that, the pressure dropped sharply at around 62 ms, but the pressure became steady as the flame was maintained. In terms of the fuel and oxidizer inlet pressures, high-frequency oscillations were observed in the oxidizer inlet pressure after ignition only under the low initial chamber pressure case. Therefore, the large difference in pressure intensity at ignition and the propagation of reverse pressure to the inlet pressure, which is upstream of the combustion chamber, suggest that the two ignition phenomena may be different.
Then, visualized observation images of CAM1 and CAM2 for each process in the high initial chamber pressure case and the low initial chamber pressure case are shown in **Figure 6**. The upper images in **Figure 6(b), (c)** are from the same test as **Figure 5(a)** and link to the explanation of the ignition and *Pc* increase at around 17 ms. Similarly, the lower images in **Figure 6(b), (c)** are from the same test as **Figure 5(b)** and are linked to the explanation of the ignition and *Pc* increase at around 57 ms. The following three major processes are shown in this figure: oxidizer single injection, oxidizer + fuel injection, and ignition process. Each image is shown with the γ value corrected to 0.5. For the high initial chamber pressure case shown in **Figure 6(a)**, the oxidizer jet started to be injected into the combustion chamber at around 4 ms. Currently, the oxidizer jet was clearly visible as a liquid column. The fuel jet was confirmed to start injecting into the combustion chamber at around 8 ms. The flame during the ignition process was observed to gradually spread over the entire combustion chamber at around 16.57 ms with a low intensity flame. In the low initial chamber pressure case shown in **Figure 6(b)**, the timing of the oxidizer and fuel injection into the combustion chamber was the same as in the high initial chamber pressure case. However, the oxidizer jet was injected in a fog-like state, without a clear jet. One of the reasons for this phenomenon is that the vapor pressure of NTO, the main component of the oxidizer MON-3, is 0.096 MPaA [22] at 20°C. When the initial pressure Pc_{ini} is lower than that, as in the low initial chamber pressure case shown in **Figure 5(b)**, the oxidizer is flash boiling. Therefore, the liquid phase of the oxidizer jet may have been atomized by the gas phase, and clear droplets could not be observed as shown in **Figure 6(b)**. In the low initial chamber pressure case, the flame during the ignition process was not a low-intensity flame, and a high-intensity flame that instantly spread to the entire combustion chamber was observed at 56.96 ms. As mentioned in the pressure history above, the flame propagation characteristics also suggested that the ignition modes in the two cases were different.

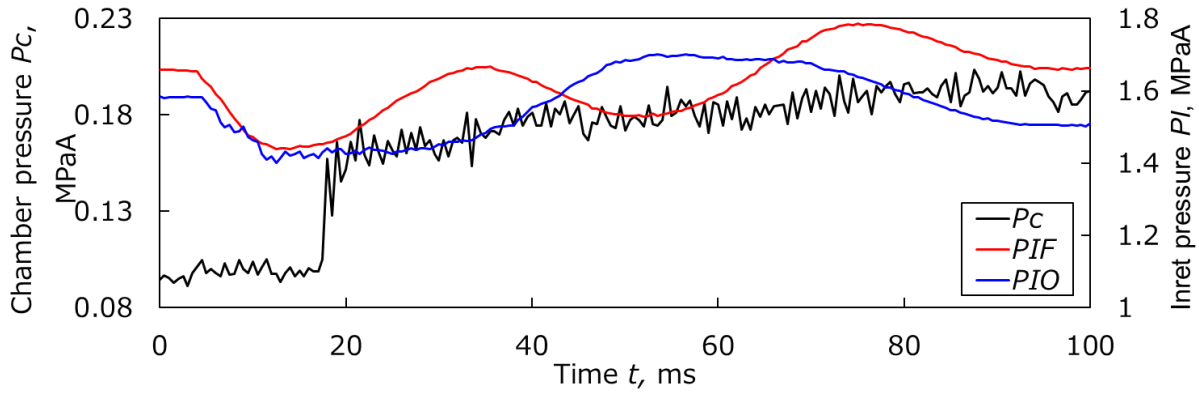

(a) high initial chamber pressure case of Pc_{ini} = 0.08 MPaA (Case 2)

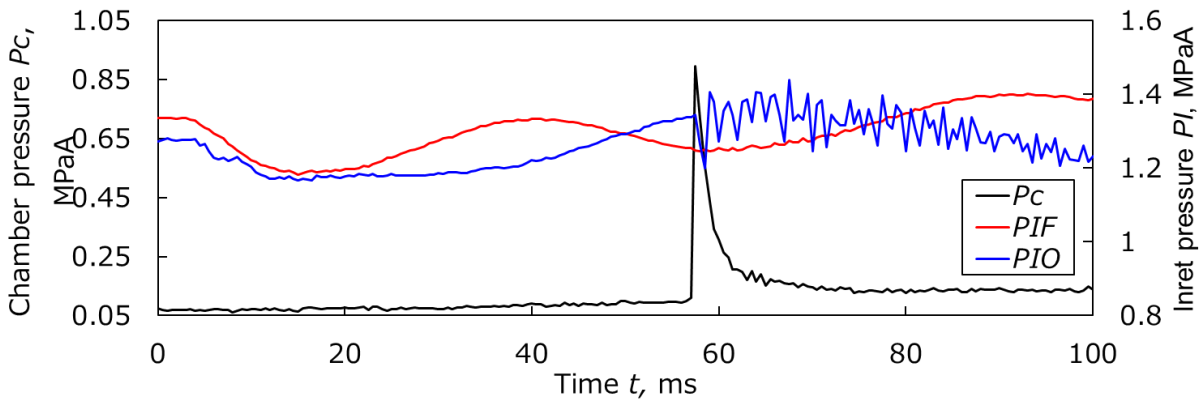

(b) low initial chamber pressure case of Pc_{ini} = 0.08 MPaA (Case 5)

Figure. 5 Comparison of combustion chamber pressure *Pc* and propellant valve inlet pressure *PI*

DOI: 10.13009/EUCASS2023-712

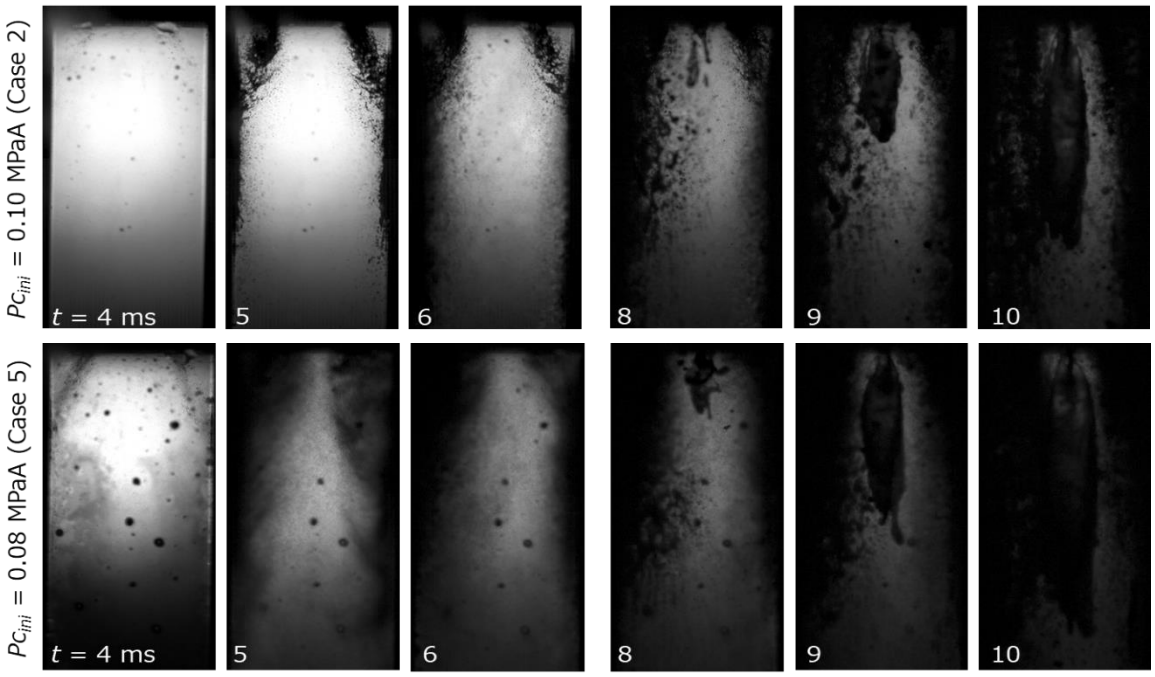

(a) Oxidizer injection state (b) Oxidizer + fuel injection state

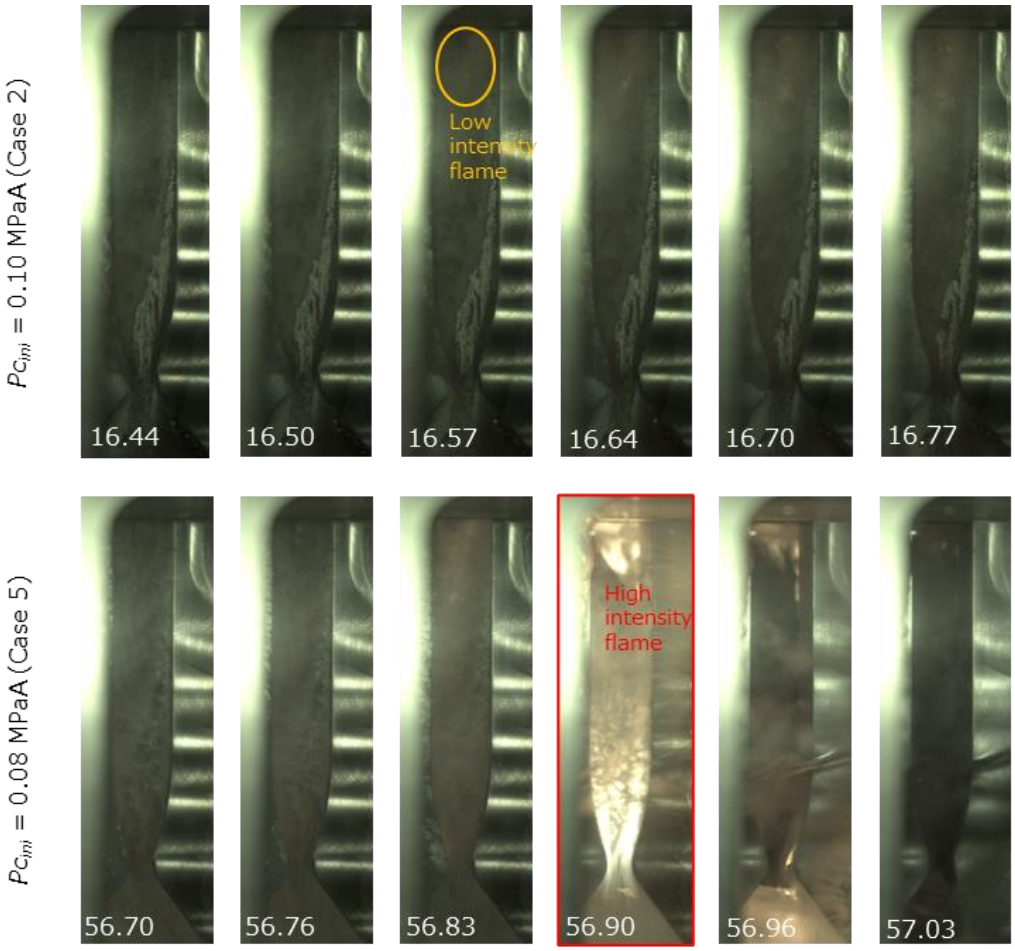

(c) Combustion state at ignition

Figure. 6 Comparison of propellant injection and combustion conditions between high and low initial chamber pressure cases

DOI: 10.13009/EUCASS2023-712

3.2 Hard start generation process

Based on the above combustion types, a total of 12 firing test case conducted in this study were classified. The peak ratio Pc_{max}/Pc_{ave} > 1.2, which is the ignition peak pressure Pc_{max} divided by the average pressure Pc_{ave} during stable combustion, was defined as the "hard start case", and other conditions were defined as the "normal start case". The average pressure during stable combustion was the average value between 10 and 20 ms after ignition. **Figure 7** shows the peak ratio for each case in firing tests using a rectangular and cylindrical combustion chamber. Among the 12 cases, 7 cases were judged to be hard start cases. The following discussion focuses on the process of occurrence and combustion conditions of these hard start cases. Focusing on the initial combustion chamber pressure Pc_{ini} in the cases where hard start occurred, hard start occurred in all cases of rectangular and cylindrical combustion chambers where Pc_{ini} = 0.08 MPaA or less. Therefore, flash boiling of the oxidizer jet at an initial pressure Pc_{ini} below the vapor pressure as described in Section 3.1 may be the main cause of the occurrence of hard start.

Since the amount of unburned fuel accumulated in the combustion chamber could determine the intensity of the hard start, the correlation between ignition delay time t_d and ignition peek pressure is shown in **Figure 8** for each combustion chamber geometry. First, the data for the pressure at ignition in the rectangular combustion chamber showed a small increase, with the peak ignition pressure Pc_{max} = 0.79 MPaA even in the case of the highest-pressure intensity. This is caused by the existence of pressure leakage at the visualized quartz glass surface in front of and behind the rectangular combustion chamber and at the metal parts on the left and right sides of the combustion chamber. As a qualitative feature, the peak ignition pressure Pc_{max} tended to increase as the ignition delay time t_d increased. In a cylindrical combustion chamber with low leakage, the peak ignition pressure Pc_{max} increased monotonically with increasing ignition delay time t_d, reaching a maximum pressure of about Pc_{max} = 3.5 MPaA. This trend suggests that the amount of unburned fuel in the combustion chamber, which changes with ignition delay time t_d, may determine the intensity of the peak ignition pressure Pc_{max} at a hard start.

To clarify the fuel accumulation state during ignition delay time t_d, the wall propellant state and the combustion chamber pressure history in a cylindrical combustion chamber are shown in **Figure 9**. The comparison image is a full view image of CAM1 with an acquisition time of 15 ms. In the O single injection case shown in **Figure 9(a)**, the oxidizer was observed as a liquid film on the wall surface. In the OF simultaneous injection case, a white turbidity region exists near the oxidizer liquid film and fuel film boundary, and it was confirmed that this region widens as one moves downstream. **Figure 9(b)** compares the combustion chamber pressure histories. The trends of the combustion chamber pressure Pc are consistent until the start of fuel injection, but immediately after the start of fuel injection, the increase trend of the combustion chamber pressure Pc becomes steeper. The above results suggest that a liquid phase of both fuel and oxidizer exists in the turbidity region, and gas is generated by the liquid-liquid reaction. The gases generated at the wall surface are unburned gas, and explosive nitrates may be formed as intermediate products [23]. In addition, it has been reported that hydrazine is stable under normal conditions, however, liquid detonation occurs when bubbles are mixed with it [24]. These results suggest that the OF liquid-liquid reaction on the wall generates unburned gas, and that the wall propellant may be a detonation source, producing a high intensity flame.

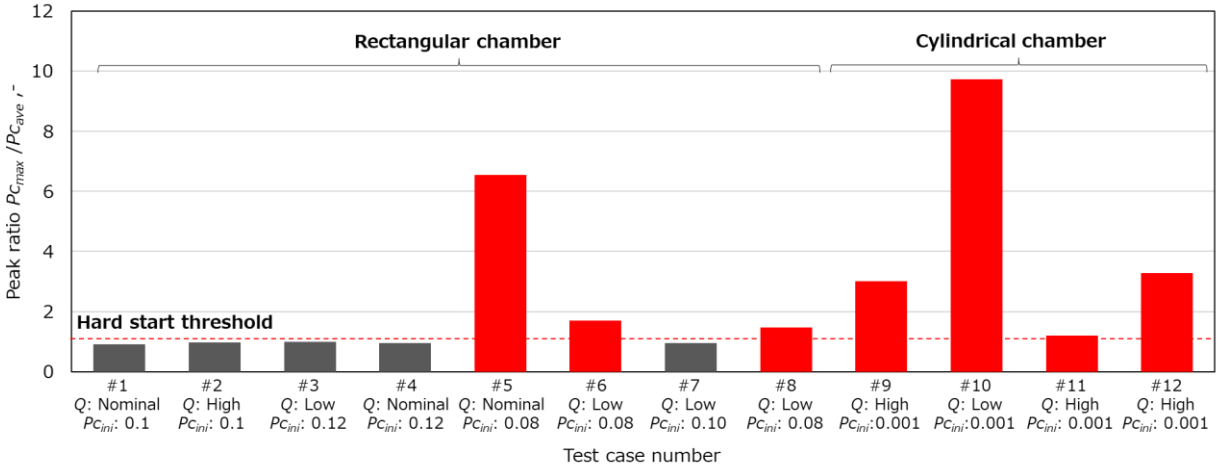

Figure. 7 Identification of hard start conditions by the ratio of ignition peak pressure Pc_{max} to the average pressure Pc_{ave} during stable combustion between 10-20 ms after ignition

DOI: 10.13009/EUCASS2023-712

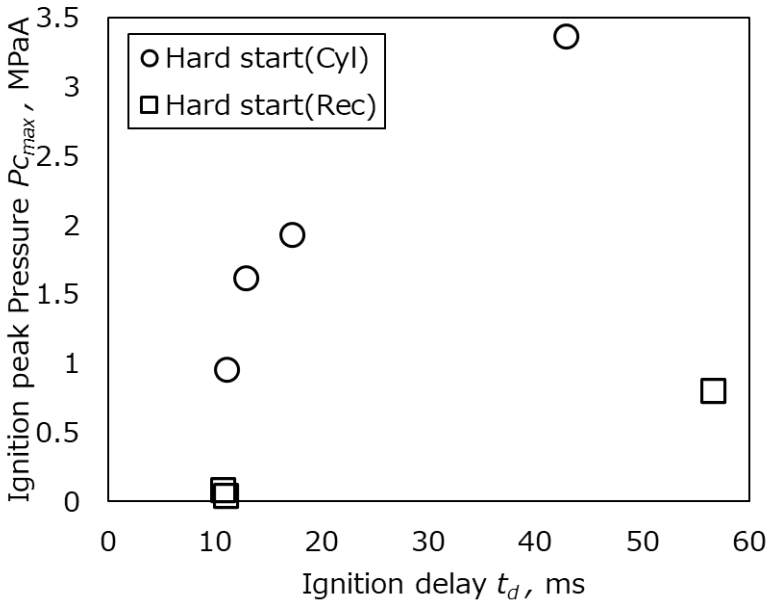

Figure. 8 Peak ignition pressure characteristics between ignition delay time t_d and peak ignition pressure Pc_{max}

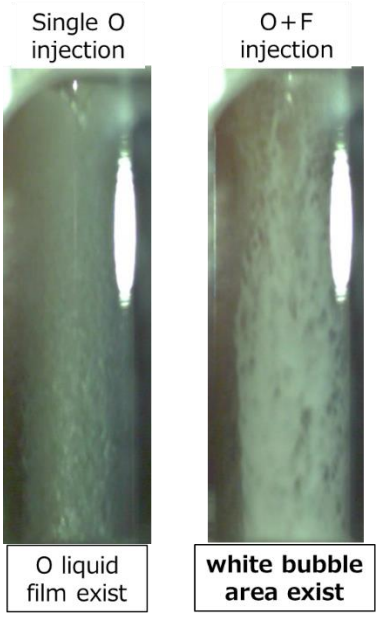

(a) Propellant condition at combustion chamber wall surface (CAM2)

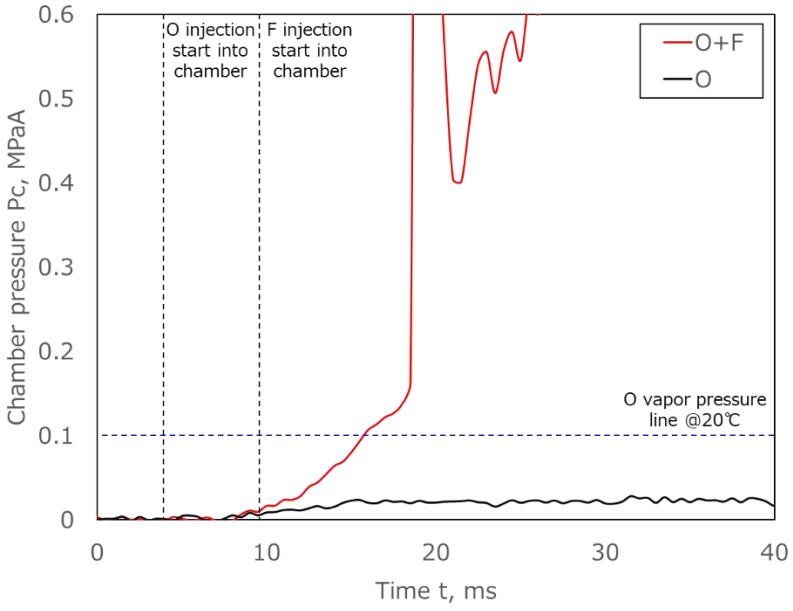

(b) Chamber pressure *Pc* time history at O single injection and O+F simultaneous injection

Figure. 9 Correlation between combustion chamber wall propellant condition and combustion chamber pressure

3.3 Flame propagation at the occurrence of hard start

To clarify the starting point of flame initiation and flame spread in the hard start case, a full view of CAM1 is shown in **Figure 10**. The images show the hard start of the OF simultaneous injection case with a cylindrical combustion chamber and high flow rate conditions. Immediately before the hard start, the combustion chamber pressure Pc is higher than the vapor pressure of the oxidizer, as shown in **Figure 9**. Therefore, the oxidizer is injected in a liquid column state, and the mixing ratio due to OF impingement is estimated to be near the rated value. Ignition point was

DOI: 10.13009/EUCASS2023-712

confirmed from the image taken at 17.28 ms, just before the high intensity flame, and low intensity flame was observed near the impingement point between the oxidizer and the fuel. This indicates that the oxidizer/fuel mixing ratio *MR* was near the rated value due to the OF impingement, which accelerated the reaction and led to the ignition. At the time of high intensity flame generation at 17.32 ms, the flame propagated over 30 mm, the visualization length of the visualized combustion chamber, in the 40 μs until the next frame. This suggests that the flame propagation velocity was more than 720 m/s. The flame propagation velocity for deflagration, which is a common combustion mode, was ~ 1 m/s. In contrast, the flame propagated very fast and was accompanied by intense spontaneous emission at the time of the hard start. This suggests that detonation, in which the flame propagation speed is supersonic, occurs in the combustion chamber. Therefore, low intensity flames were first generated and propagated near the impingement point, and then the flames propagated to the products of the wall reaction described in section 3.2, and the energy input caused the detonation in the combustion chamber.

As shown in section 3.2, unburned product gas is considered to accumulate in the combustion chamber and inside the pressure port due to the OF-liquid-liquid reaction on the combustion chamber wall. Therefore, a numerical analysis was used to reproduce the combustion conditions at the time of the hard start. For simplicity, a numerical analysis was performed assuming that the premixture of N2H4/MON-3 was filled. **Figure 11(a)** shows the time histories of pressure contours in the combustion chamber and pressure port. Even when the high-temperature, high-pressure spot of the detonation source spreads and propagates into the pressure port, the temperature behind the shock wave remains high, indicating that the detonation is propagating. Although the lattice resolution is not sufficient because only a few points are available for the half-reaction distance behind the shock wave, **Figure 11(b)** shows that the detonation velocity obtained by the analysis is about 2800 m/s, which is close to the CJ detonation velocity of 2640 m/s obtained by NASA-CEA.

Figure 12 compares the pressure histories measured at a single point through the pressure port for the shock wave analysis case and the combustion analysis cases (1/2 Case and 1/4 Case). For the shock wave analysis case, the first pressure peak indicates a shock impact on the pressure measurement surface, followed by a gradual attenuation trend; the second and subsequent pressure peaks indicate reflected wave impact on the pressure port inlet side. The peak value of the analysis was about 0.38 MPaA, which was lower than the measured peak ignition pressure Pc_{max} = 1.88 MPaA, and the pressure attenuation was also faster than the measured result. Therefore, the hypothesis that gas detonation occurred inside the combustion chamber and the shock wave propagated through the pressure port was not correct. Then, for the combustion analysis case, the initial pressure peaks are much higher than those in the shock wave analysis case, 19.3 MPaA in the 1/2 case and 14.8 MPaA in the 1/4 case. The pressure attenuation in the analysis is faster than in the measurement. However, the period of the pressure peak due to the reflected wave is also shorter. Therefore, the average pressure attenuation appears to be close to that of the measurement. In addition, the pressure measurement in this study is at 2000 Hz, and it is likely that the high-frequency phenomena seen in the analysis were not measured. Therefore, a comparison of the pressure history between the numerical analysis and the measurement suggests that the flame at the time of the hard start in the measurement may be an ignition with detonation. The hypothesis that detonation occurred in the pressure conduit at the time of the hard start is not yet fully proven, because the sampling frequency is too small to compare with the numerical analysis results. Since liquid-phase detonation may have also occurred, comparison with the test results will be continued.

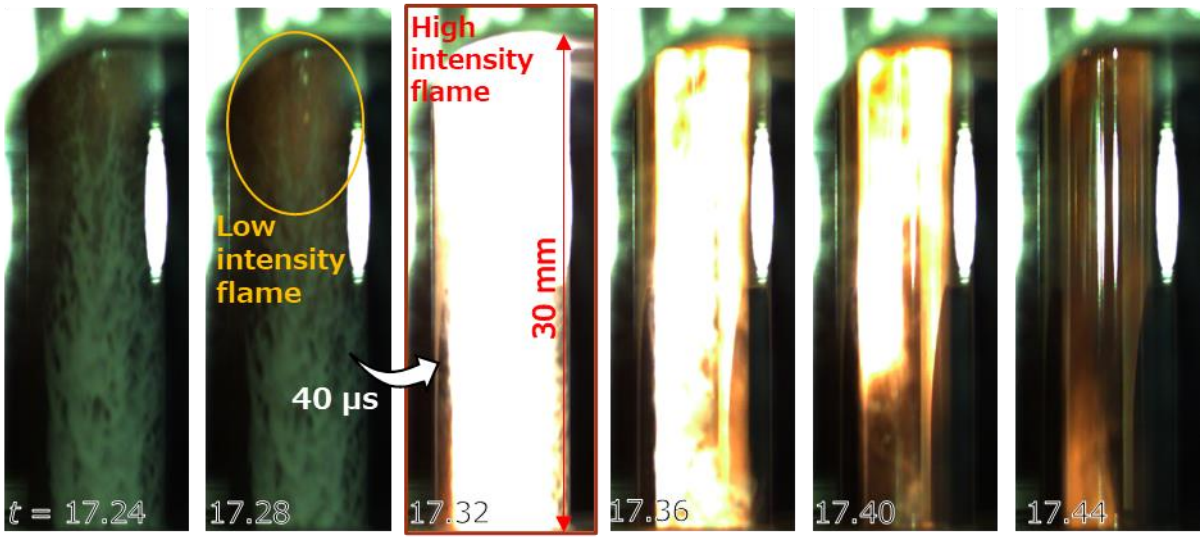

Figure. 10 Observed images of ignition starting point and high-intensity flame development during ignition

DOI: 10.13009/EUCASS2023-712

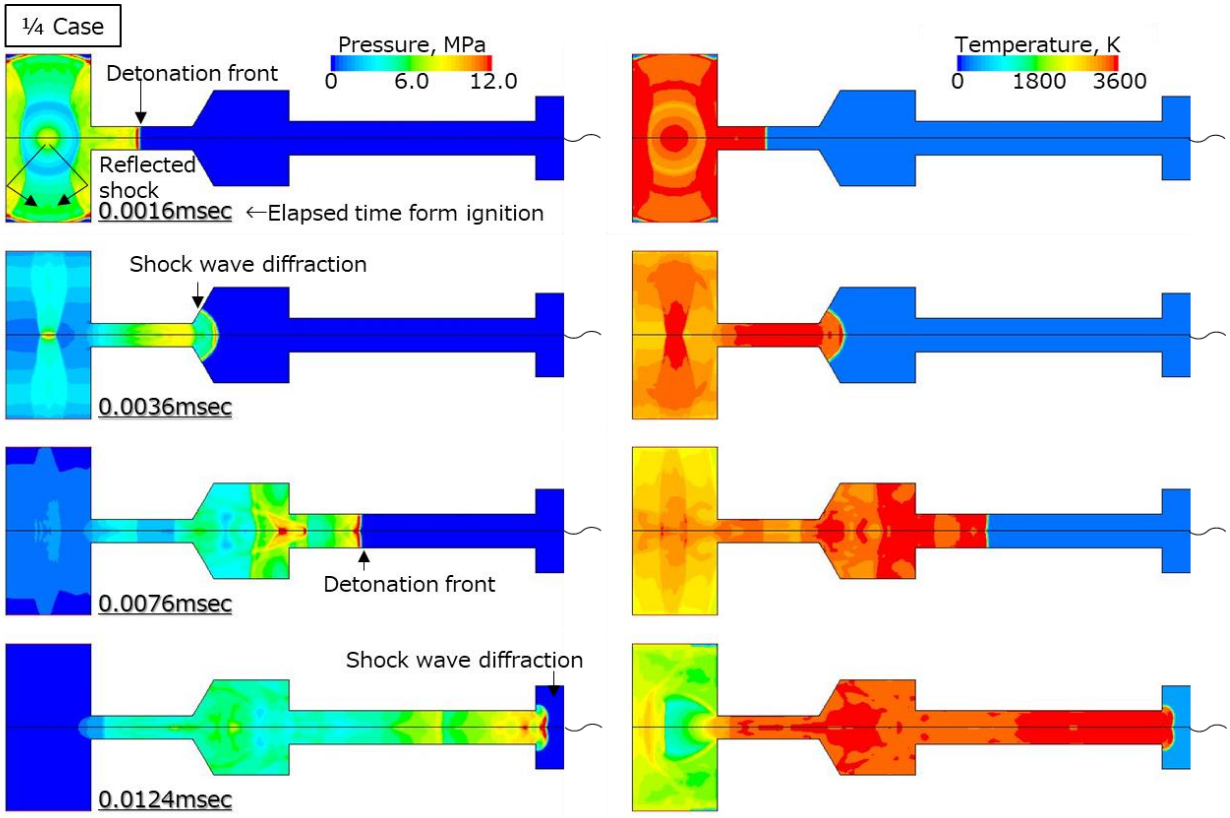

(a) Time history of pressure and temperature contours in combustion chamber and pressure port

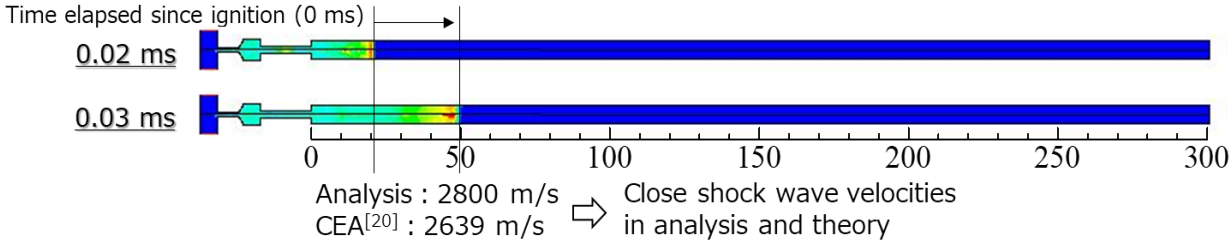

(b) Shock wave velocity comparison

Figure. 11 Numerical analysis of detonation propagation in combustion chamber and pressure port

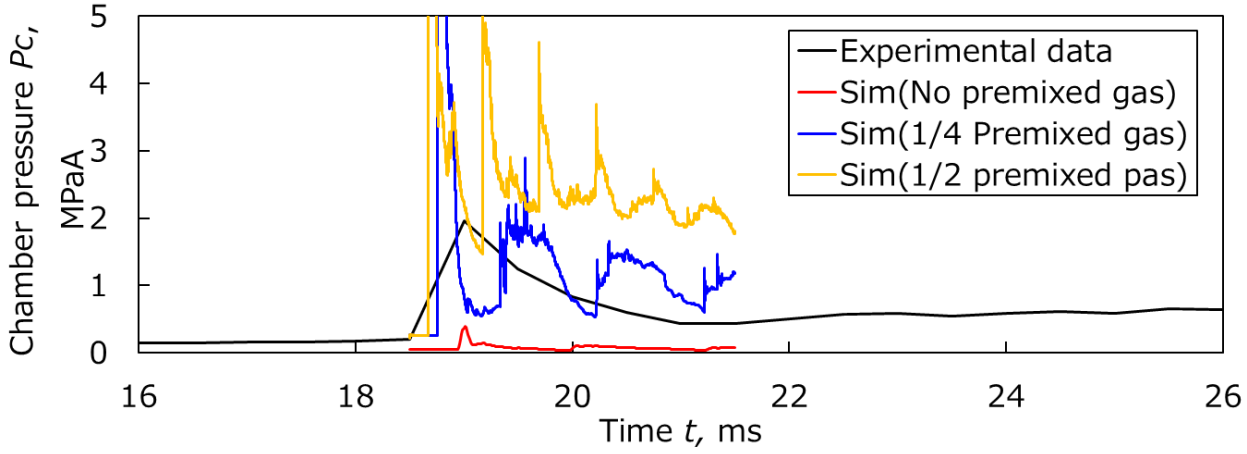

Figure. 12 Pressure history of hard start by measurement and numerical simulation

DOI: 10.13009/EUCASS2023-712

3.4 Estimation of hard start generation process

Based on the findings of the previous sections, a hard start generation process is estimated in **Figure 13**.
First, as in (i), the oxidizer is injected into the combustion chamber ahead of the fuel. At this time, the pressure in the manifold and combustion chamber is close to a vacuum. Therefore, the oxidizer with high vapor pressure is injected with flash boiling. The pressure in the manifold and combustion chamber gradually increases with the vaporization of the oxidizer.
Second, fuel is injected into the combustion chamber following the oxidizer, as shown in (ii). At this time, the pressure in the manifold and combustion chamber is not higher than the vapor pressure of the oxidizer. Therefore, the mixing ratio due to OF impingement is insufficient, and ignition is not achieved. In addition, the liquid-liquid reaction of the O-jet and F coolant film impinging on the combustion chamber wall produces product gas. This further increases the pressure in the manifold and combustion chamber.
Third, when the manifold and combustion chamber are above the vapor pressure of the oxidizer, as in (iii), the oxidizer jet stabilizes in the liquid phase. This causes the mixing by OF impingement to reach a sufficient state for the combustion reaction. Therefore, a chain of combustion reactions occurs, and a low-intensity flame is produced near the impingement point.
Fourth, as in (iv), detonation with a high intensity flame occurs instantaneously after the low intensity flames. The detonation is considered to occur when unburned fuel accumulated on the combustion chamber wall becomes detonable due to nitrate formation and other factors. The detonation is then considered to propagate through the combustion chamber while consuming the premixed gas.
Based on the above hard start process, to avoid hard start, it is considered effective to accelerate mixing by increasing the injection momentum, improve the combustion chamber pressure increase rate by decreasing the combustion chamber volume, and preliminarily increase the combustion chamber pressure by operating the oxidizer leads.

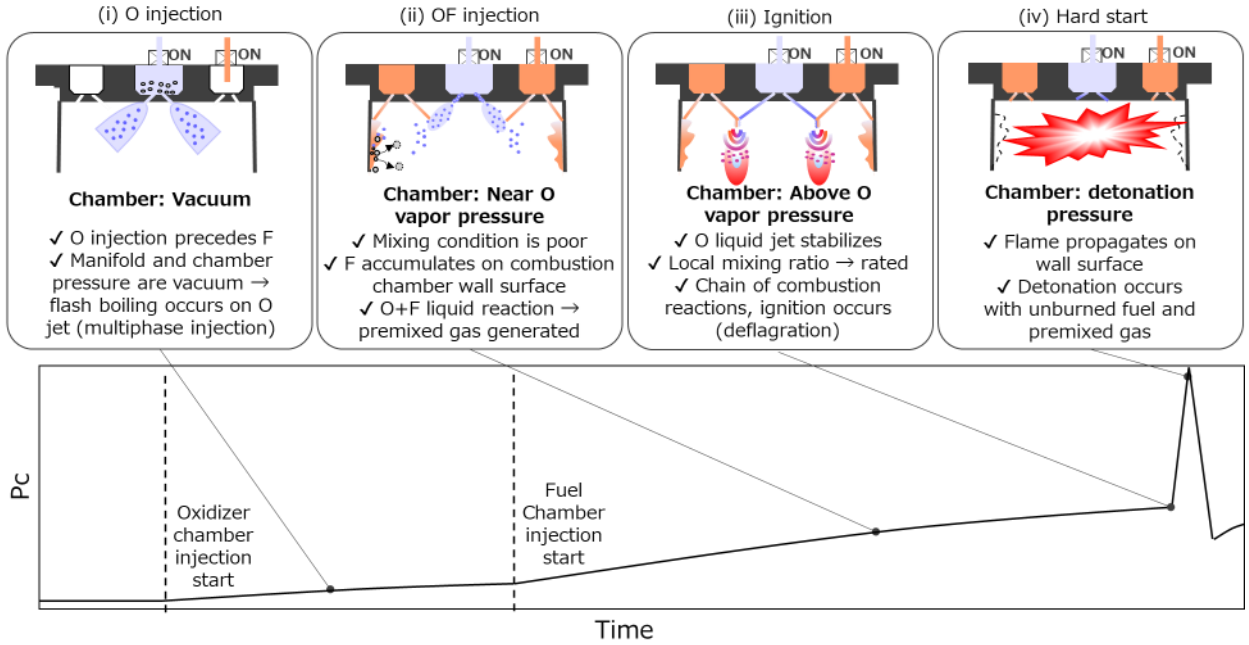

Figure. 13 Estimation scenario from propellant injection to hard start

4. Conclusion

The objective of this study is to clarify the hard start generation process of a bipropellant thruster by observing physical phenomena during the start up transient, and the following findings were obtained. Based on the ratio of ignition peak pressure to average stable combustion pressure, it was determined that a hard start was observed in a vacuum condition. The hard start is most likely to occur when the initial combustion chamber pressure is below the oxidizer vapor pressure. The ignition peak pressure due to hard start increases monotonically with increasing ignition delay time, suggesting that this is caused by the accumulation of unburned fuel on the inner wall of the combustion chamber. During the ignition delay time, the OF liquid-liquid reaction generates gases on the inner wall of the combustion chamber,

DOI: 10.13009/EUCASS2023-712

suggesting that the wall propellant is likely to induce detonation. The flame at the time of hard start was suggested detonation. Numerical simulation of the combustion state at the time of the hard start suggests that gas detonation may have propagated when the premixed gas was filled to about 1/4 of the pressure conduit volume. Based on these knowledges, a hard start generation process was estimated. This understanding of hard start and construction of the generation process will contribute to the development of reliable thrusters with improved starting stability in the future.

References

[1] Campagnola, S., Yam, C. H., Tsuda, Y., Ogawa, N., and Kawakatsu, Y., "Mission Analysis for the Martian Moons Explorer (MMX) Mission", *Acta Astronautica*, Vol. 146, 2018, pp. 409-417.

[2] Takata, S., Sasaki, H., Fukatsu, T., and Sugimori, K., "The Compatibility Evaluation Method of the 500N & 120N Japanese Bi-Propellant Thrusters with the HTV System & Operation Design", *Transactions of the Japan Society for Aeronautical and Space Sciences*, Vol. 12, No. ists29, 2014, pp.7-15.

[3] Tani, H., Terashima, H., Koshi, M., and Daimon, Y., "Hypergolic ignition and flame structures of hydrazine/nitrogen tetroxide co-flowing plane jets", *Proceedings of the Combustion Institute*, Vol.35, 2015, pp.2199-2206.

[4] Daimon, Y., Negishi, H., Tani, H., Matsuura, Y., Iihara, S., and Takata, S., "Flow Field and Heat Transfer Analysis in a MON/MMH Bipropellant Rocket Engine", *International Journal of Energetic Materials and Chemical Propulsion*, Vol. 16, No. 3, 2017, pp. 263-280.

[5] Kang, H., Lee, E., and Kwon, S., "Suppression of Hard Start for Nontoxic Hypergolic Thruster Using H2O2 Oxidizer", *Journal of Propulsion and Power*, Vol. 33, No. 5, 2017, pp.1111-1117.

[6] Sato, M., Kusaka, K., Tadano, M., Miyajima, H., Kobayashi, H., "Hard Start Problem of the Apogee Engine for the ETS-VI", *Technical Report of National Aerospace Laboratory*, NAL TR-1036, 1989, (In japanese).

[7] Dambach, M. E., Solomon, Y., Heister, D. S., and Pourpoint, L. T., "Investigation into the Hypergolic Ignition Process Initiated by Low Weber Number Collisions", *Journal of Propulsion and Power*, Vol. 29, No. 2, 2013, pp. 331-338.

[8] Venkatesh, B. P., Osborne, L., Fitzpatrick, M., Hollinbeck, M., and Barnes, D., "Pulse Performance Analysis of a 45 Newton Additively Manufactured Bipropellant Thruster", *Journal of Propulsion and Power*, Vol.37, No.6, 2021, pp.832-841.

[9] Hearn, C. H., "Thruster requirements and concerns for bipropellant blowdown systems", *Journal of Propulsion and Power*, Vol. 4, No. 1, 1988, pp.47-52.

[10] Boorady, A. F., and Douglass, A. D., "AGENA GEMINI ROCKET ENGINE - HARD START PROBLEM RESOLVED DURING PROJECT SURE FIRE", *Simulation and Support Conference*, No.67, 1966, 259.

[11] Fujii, G., Daimon, Y., Inoue, C., Shiraiwa, D., Tanaka, N., and Furukawa, K., "Visualization of Pulse Firing Mode in Hypergolic Bipropellant Thruster", *Journal of Propulsion and Power*, Vol.36, No.5, 2020, pp.677-684.

[12] Hatai, K., and Nagata, T., "Quantitative Clarification of Stable Ignition Region for HKP110 Green Hypergolic Bipropellant", *Aerospace*, Vol. 9, No. 3, 2022, pp.129.

[13] Miron, Y., and Perlee, H. E., "The Hard Start Phenomena in Hypergolic Engines Volume III. Physical and Combustion Characteristics of Engine Residues", *NASA Technical Report*, NASA CR-140361.

[14] Miron, Y., and Perlee, H. E., "The Hard Start Phenomena in Hypergolic Engines Volume IV. The Chemistry of Hydrazine Fuels and Nitrogen Tetroxide Propellant Systems", *NASA Technical Report*, NASA CR-140360.

[15] Matsuura, Y., Iihara, S., and Tashiro, Y., "Hypergolic Propellant Ignition Phenomenon Associated with Two-Phase Oxidizer Flow Injection", *Journal of Propulsion and Power*, Vol.30, No.5, 2014, pp.1399-1409.

[16] Fujii, G., Daimon, Y., Tominaga, K., Nagata, T., Matsuura, Y., and Kano, Y., "Visualization of Hard Start Phenomena in Hypergolic Bipropellant Thrusters", *Space Propulsion 2022*, SP2022_081.

[17] Inoue, C., Takeuchi, Y., Nozaki, K., Himeno, T., Watanabe, T., Fujii, G., Daimon, Y., "Unified Length Scale of Spray Structure by Unlike Impinging Jets", *TRANSACTIONS OF THE JAPAN SOCIETY FOR AERONAUTICAL AND SPACE SCIENCES*, Vol.62, No.4, 2019, pp.213-218.

[18] Inoue, C., Oishi, Y., Daimon Y., Fujii, G., Kawatsu., K, "Direct Formulation of Bipropellant Thruster Performance for Quantitative Cold-Flow Diagnostic", *Journal of Propulsion and Power*, Vol.37, No.6, 2021, 842-849.

[19] Oishi, Y., Tauchi, S., and Inoue, C., "Unsteady Stream-Tube Model for Pulse Performance of Bipropellant Thrusters", *Journal of Propulsion and Power*, Vol.39, No.1, 2023, pp.3-10.

[20] Gordon, S., and McBride, J. B., "Computer Program for Calculation of Complex Chemical Equilibrium Compositions and Applications. Part 1: Analysis", *NASA Reference Publications 1311*, Lewis Research Center, 1994, 19950013764.

[21] Daimon, Y., Terashima, H., and Koshi M., "Chemical Kinetics of Hypergolic Ignition in N2H4/N2O4-NO2 Gas Mixtures", *Journal of Propulsion and Power*, Vol. 30, No. 3, 2014, pp.707-716.

DOI: 10.13009/EUCASS2023-712

[22] McCarty, D., R., Steurer, U., H., Daily, M., C., “THE THERMODYNAMIC PROPERTIES OF NITROGEN TETROXIDE”, *National Bureau of Standards*, 1986, NBSIR86-3054.
[23] Izato, Y., Shiota, K., Miyake, A., “A detailed mechanism for the initial hypergolic reaction in liquid hydrazine/nitrogen tetroxide mixtures based on quantum chemistry calculations”, *Combustion and Flame*, Vol.229, 2021, pp.111389.
[24] Schmidt, W., E., “Hydrazine and Its Derivatives: Preparation, Properties, Applications”, *Wiley-Interscience*, 2001.